RSC Advances

ROYAL SOCIETY OF CHEMISTRY

www.rsc.org/advances

Influence of sintering additives on densification and Li^+ conductivity of Al doped $Li_7La_3Zr_2O_{12}$ lithium garnet

Narayanasamy Janani, C. Deviannapoorani, L. Dhivya and Ramaswamy Murugan*

Corresponding Author

Department of Physics, Pondicherry University, Puducherry - 605 014, India.

*Phone: 91 413 2654782. Email: moranamurugan.phy@pondiuni.edu.in

Abstract

Garnet-like structured solid electrolyte $Li_7La_3Zr_2O_{12}$ (LLZ) in cubic phase has received unique attention due to its high total (bulk + grain-boundary) Li^+ conductivity combined with good chemical stability against lithium metal and commercial electrodes. In addition to the stabilization of high Li^+ conductive cubic phase, the dense microstructure related to grains and grain-boundaries is also a critical issue for the successful application of LLZ as solid electrolyte membrane in all-solid-state lithium and lithium-air batteries. In this work, preparation of high Li^+ conductive 0.9 wt.% Al doped cubic LLZ i.e. $Li_{6.16}Al_{0.28}La_3Zr_2O_{12}$ (Al-LLZ) by modified sol-gel technique and the influence of sintering additives on the density and total (bulk + grain-boundary) Li^+ conductivity of the Al-LLZ is investigated. The present work reveals that among the three chosen sintering additives Li_3BO_3, Li_3PO_4 and Li_4SiO_4, the Li_4SiO_4 appears to be a better sintering additive for the enhancement of the total (bulk + grain-boundary) Li^+ conductivity and density of Al-LLZ. Among the investigated samples, Al-LLZ added with 1wt.% of Li_4SiO_4 sintered at 1200 °C exhibits maximized total (bulk + grain-boundary) Li^+ conductivity of 6.1 x 10^{-4} Scm^{-1} at room temperature (33 °C) along with the maximized density of 4.86 gcm^{-3} (relative density of 96%).

KEYWORDS: Garnet type oxides; Sol-gel; Sintering agents; Densification; Raman spectroscopy.

1 Introduction

The huge demand for electrical energy storage devices with high energy density promotes the intensive research in advanced lithium-ion (Li^+) and lithium-air battery technologies. Solid fast Li^+ conductors are believed to be potential candidate to replace the organic liquid electrolytes and thereby improve the safety of next generation high energy density lithium batteries. In the last few years, a series of garnet-like structured inorganic solid electrolytes have been investigated as potential fast Li^+ conductors for all-solid-state lithium battery application.[1-3] Among the various lithium garnets, $Li_7La_3Zr_2O_{12}$ (LLZ) reported by Murugan et al.[4] has received special attention due to its high total (bulk + grain-boundary) Li^+ conductivity in the order of 10^{-4} Scm^{-1} at 25 °C, combined with good chemical stability against lithium metal and commercial electrodes. LLZ has two different crystal phases, viz.; cubic and tetragonal phase.[4-8] The total (bulk + grain-boundary) Li^+ conductivity was found to be two orders of magnitude higher for cubic phase than that of the tetragonal phase LLZ.[4] Earlier studies suggested that the incorporation of Al from alumina crucibles into LLZ pellet during the high-temperature solid state synthesis helps to stabilize the cubic phase against the tetragonal one.[8-11] Systematic studies on LLZ suggested that the phase stability of high Li^+ conductive cubic phase is influenced by Li concentration and also by the Al inclusion. Buschmann et al. revealed that the incorporation of 0.9 wt.% of Al (28 mol% of Al per mol $Li_7La_3Zr_2O_{12}$) from the Al_2O_3 crucible helps to stabilize the LLZ sample in high Li^+ conductive cubic phase.[11] Rangasamy et al. indicated that the optimized content of Al and Li required to form cubic LLZ in boron nitride coated Al_2O_3 crucible was 0.24 moles and 6.24 moles, respectively.[12] Also the incorporation of a major viscosity and devitrification agent Al from the crucible helps to form favourable Li^+ conducting thin layer in the grain-boundary regions through Li_2O-ZrO_2-Al_2O_3 eutectic. If the Al^{3+} replace some of the Li^+ which may lead to

Li^+ extraction from the bulk (via charge compensation for the above substitution) into the grain-boundary region for the formation of favourable Li^+ conducting thin layer and also the simultaneous increased number of empty structural sites in the lattice could permit increased Li^+ mobility and thus conductivity.

Preparation of LLZ by conventional solid state synthesis technique requires high reaction temperature, long duration of sintering along with the intermittent grinding and repeated heat treatments.[4] It is also difficult to control the chemical stoichiometry of the lithium garnets through solid state synthesis due to volatile nature of lithium at high temperature. Attempts were made to overcome these difficulties by switching over to wet chemical techniques.[13-18] Homogeneous mixing of reactants at molecular level, relatively lower reaction temperature and shorter sintering time are the main advantages of this method over the solid state method. The powder obtained from the wet-chemical method generally shows better performance due to their higher homogeneity in composition, finer crystal size, higher purity and surface area.

Preparation of nanocrystalline cubic phase lithium garnets $Li_5La_3Ta_2O_{12}$ and $Li_5La_3Bi_2O_{12}$ through sol-gel method by sintering the gels at 973 K and 923 K, respectively, were first reported by Gao et al.[13,14] Later Shimonishi et al. reported the preparation of lithium garnets with nominal formulae $Li_6La_3Zr_2O_{11.5}$ in cubic phase and $Li_7La_3Zr_2O_{12}$ in tetragonal phase using sol-gel method by sintering the samples at 1180 K and 800 K, respectively.[15] Kokal et al. reported the preparation of LLZ in cubic phase at 973 K by modified sol-gel technique and also they reported cubic to tetragonal modification of LLZ at 997 K.[16] The stabilization of cubic phase LLZ by the addition of Al through a polymerized complex method was later reported by Jin et al.[17] The preparation of LLZ and Al doped LLZ at lower sintering temperature by modified sol-gel technique using butan-1-ol and 2-propanol as surfactants was also reported.[18]

In addition to the stabilization of high Li^+ conductive cubic phase, the dense microstructure related to grains and grain-boundaries is also a critical issue for the successful application of LLZ as solid electrolyte membrane in all-solid-state lithium and lithium-air battery technologies. The dense microstructure is expected to enhance the total (bulk + grain-boundary) Li^+ conductivity by reducing the grain-boundary resistance and also expected to barricade the dendritic growth during lithium deposition. Ceramics are usually sintered at elevated temperatures for longer duration to yield high dense pellets. The sintering temperature of ceramics can be reduced by utilizing suitable sintering aids with a low melting temperature. Even if the melting point of sintering aid is slightly higher than the sintering temperature it may help to sinter the ceramics through the formation of eutectic composition. Recently, an attempt has been made to enhance the density of LLZ by the addition of Li_3BO_3[19] and Ta doped LLZ by the addition of Li_3PO_4 and Li_2O.[20-22]

In this work, systematic investigations have been carried out on the preparation of high Li^+ conductive 0.9 wt.% of Al doped LLZ i.e. $Li_{6.16}Al_{0.28}La_3Zr_2O_{12}$ (Al-LLZ) in cubic phase by modified sol-gel technique and also the influence of sintering additives Li_3BO_3, Li_3PO_4 and Li_4SiO_4 on the density and total (bulk + grain-boundary) Li^+ conductivity of Al-LLZ is investigated.

2 Experimental section

2.1 Synthesis

$LiNO_3$ (Sigma-Aldrich), $La(NO_3)_3 \cdot 6H_2O$ (Sigma-Aldrich), $ZrO(NO_3)_2 \cdot xH_2O$ (Sigma-Aldrich) and $Al(NO_3)_3 \cdot 9H_2O$ (Sigma-Aldrich) with 99.9% purity were used as reactants for the preparation of $Li_7La_3Zr_2O_{12}$ (LLZ) and 0.9 wt.% of Al doped $Li_7La_3Zr_2O_{12}$ (Al-LLZ) by

modified sol-gel technique. Thermogravimetric (TG) and Powder X-ray Diffraction (PXRD) analysis have revealed that as received $ZrO(NO_3)_2 \cdot xH_2O$ corresponds to that of $ZrO(NO_3)_2 \cdot 5H_2O$. The appropriate amount of $LiNO_3$ (10 wt.% excess was added to compensate the expected Li loss), $La(NO_3)_3 \cdot 6H_2O$ and $ZrO(NO_3)_2 \cdot 5H_2O$ were dissolved in distilled water for the preparation of LLZ and additionally appropriate amount of $Al(NO_3)_3 \cdot 9H_2O$ were added for the preparation of $Li_{6.16}Al_{0.28}La_3Zr_2O_{12}$ (Al-LLZ). To the above precursors, citric acid and butan-1-ol were added as chelating and surface active agent, respectively. The above solutions were stirred well for 24 h with simultaneous heating at 60 °C for the evaporation of solvent in order to get a transparent yellow gel. The gel was heated at 250 °C for 1 h. The resultant brown powder was ground well and calcined at various temperatures.

Li_3BO_3 and Li_4SiO_4 were prepared using the procedure given in the literature.[19,23] The Al-LLZ powder obtained by annealing the brown precursor at 900 °C for 12 h was ball-milled with 1wt.% of Li_3BO_3, Li_3PO_4(Sigma-Aldrich) and Li_4SiO_4 independently for about 6 h using a Pulverisette 7, Fritsch, Germany. The mixed powders were pressed into pellet and sintered at 900 °C for 36 h in a closed alumina crucible. In addition to this the Al-LLZ powder mixed with 1wt.% of Li_3PO_4 and with 1wt.% of Li_4SiO_4 were pressed into pellet and sintered in a closed alumina crucible at 1200 °C for 12 h by covering the pellets with the same mother powder to reduce the possible lithium loss. The detailed procedure for the preparation of investigated samples is shown in Fig. 1.

2.2 Characterization

The phase purity of the prepared samples were examined by Powder X-ray Diffraction (PXRD) using X'pert PANalytical X-ray diffractometer with Cu-K_α radiation of λ = 1.5418 Å from 2θ =

10° to 70° with a step size of 0.025°. Scanning Electron Microscope (SEM; HITACHI S-3400N) was used to examine the morphology of the prepared samples. A field-emission scanning electron microscope SU8000 Family Ultra-High Resolution (FE-SEM) equipped with Energy dispersive X-ray detector (EDX) was used to obtain microstructure of the fractured surface of the pellet. The densities of the sintered pellets were measured at room temperature (33 °C) with the Archimedes principle using deionised water as the immersion medium. Confocal micro-Raman spectroscopic investigations on the prepared samples at room temperature in the range 75-1000 cm^{-1} were performed using a Renishaw in via Reflex spectrometer having a 50 mW internal Ar^{+} laser source at the excitation wavelength of 514 nm. Electrical conductivity measurements of the sintered pellets were performed using Li^{+} blocking Au-electrodes (Au paste cured at 600 °C for 1 h) in the frequency range (20 Hz to 15 MHz) using a Precision Impedance analyzer (Wayne Kerr 6500B) in the temperature range from room temperature (33 °C) to 240 °C.

3 Results and discussion

3.1 Structural analysis

The PXRD patterns of LLZ and Al-LLZ precursors sintered at various temperatures along with the reported cubic[4] and tetragonal phase[6,24] are shown as Fig. 2. The PXRD pattern of LLZ brown precursor annealed at 700 °C shown as Fig. 2 (a) indicated the formation of pyrochlore $La_2Zr_2O_7$ as major phase. Few small extraneous reflections in the trace just above the background level are observed as shown in Fig. 2 (a), which may correspond to residual minor La_2O_3 phase. By increasing the sintering temperature to 800 °C and 900 °C, the residual lithium and lanthanum oxides react with the $La_2Zr_2O_7$ phase to form the tetragonal phase LLZ as shown in Fig. 2 (b) and 2 (c). As the sintering temperature further increased to 1000 °C the formation of

$La_2Zr_2O_7$ as secondary phase was observed (not shown). The PXRD pattern of the LLZ precursor sintered at 800 °C in tetragonal phase exposed to humid conditions results in the formation of cubic like garnet phase as shown in Fig. 2 (d). The PXRD patterns of LLZ exposed to humid condition (Fig. 2 (d)) exhibit broadened diffraction peaks and also shift in peak position towards the lower diffraction angle compared with that of reported high conductive cubic LLZ.[4] The PXRD pattern of Al-LLZ precursor sintered at 900 °C shown as Fig. 2 (e) revealed the cubic phase similar to the reported high conductive cubic LLZ[4] as major phase along with the minor $LaAlO_3$ phase. The PXRD pattern of Al-LLZ precursor sintered at 1200 °C (Fig. 2 (f)) indicates the formation of well crystallized single phase similar to that of the reported high conductive cubic LLZ.[4] The lattice constant of Al-LLZ sintered at 1200 °C was found to be 12.9602(2) Å.

Raman scattering is a very useful technique for acquiring structural information on the Li^+ conductive oxides. For several lithium garnets and lithium metal oxide materials, the internal modes of LiO_6 and LiO_4 were appeared in the region 200-300 cm^{-1} and 350-500 cm^{-1}, respectively.[25,26] Raman studies carried out earlier on LLZ, predicted the bands between 100 cm^{-1} and 150 cm^{-1} corresponds to vibration of the heavy La cation and the band observed around 640 cm^{-1} correspond to the Zr-O bond stretching.[27] The considerable mixing between internal modes of LiO_4, LiO_6 and the other coordinated groups presented in the structure leads to complication in the interpretation of the Raman spectra of lithium garnets.

The major difference observed between the Raman spectra of cubic and tetragonal phase of LLZ was the presence of larger number of Raman peaks or bands for tetragonal than that of the cubic phase particularly in the region 200-500 cm^{-1}. The LLZ crystallized in tetragonal phase (space group $I4_1/acd$; No. 142) is an ordered structure with lithium on tetrahedral 8*a* site and octahedral 16*f* and 32*g* sites.[6] On the other hand the LLZ stabilized in cubic phase (space

group $Ia\bar{3}d$; No. 230) is disordered on both the 24*d* Li(1) tetrahedral site and 96*h* Li(2) octahedral sites.[7] Group theory analysis predicts 81 modes for the tetragonal (space group $I4_1/acd$; No. 142) and 51 modes for the cubic (space group $Ia\bar{3}d$; No. 230) $Li_7La_3Zr_2O_{12}$ garnet, respectively. The broad spectral features of the cubic garnet in the region 200-500 cm^{-1} might be due to the static or dynamic disorder of highly mobile Li^+ compared to the ordered arrangement in tetragonal phase.[28] The broad and fairly overlapping bands associated to degenerate Raman modes observed in the intermediate-energy region of cubic LLZ partly split in tetragonal LLZ phase, due to its lower symmetry, thus originating a higher number of observed peaks.

The Raman spectra of LLZ and Al-LLZ precursors sintered at various temperatures along with the reported cubic and tetragonal phase[28,29] are shown in Fig. 3. Raman spectrum of LLZ brown precursor sintered at 700 °C shown as Fig. 3 (a) also indicated the formation of pyrochlore $La_2Zr_2O_7$ phase as revealed by the PXRD investigation. Raman spectra also confirms the formation of LLZ in tetragonal phase for the precursor sintered at 800 °C and 900 °C as shown in Fig. 3 (b and c). The close observation of Raman spectrum of LLZ precursor sintered at 800 °C and exposed to humid conditions (Fig. 3 (d)) revealed that it is neither high conductive cubic nor tetragonal LLZ. However the PXRD pattern of the LLZ precursor sintered at 800 °C and exposed to humid conditions indicated the formation of cubic like garnet phase (Fig. 2 (d)). The nature of the high and low temperature cubic garnet is totally different: the one found above the tetragonal to cubic phase transition does not involve major change in the stoichiometry, whereas the cubic phase formed at low temperature involve change in the stoichiometry.[27] Tetragonal phase lithium garnets were reported to be sensitive to ambient conditions, especially when exposed to humid conditions.[27] The formation of cubic phase at lower temperature is found to depend upon two hydration mechanisms; the first one involves the insertion of water

molecules into the garnet structure and the second is protonation through the H^+/Li^+ exchange mechanism.[27] An increase in the cell parameter observed for the LLZ sample sintered at 800°C and exposed to humid conditions (13.0025(2) Å) compared to that of reported cubic LLZ (12.9682(6) Å)[4] sintered at elevated temperatures around 1200 °C in alumina crucible might be due to the replacement of Li-O bonds by O–H···O hydrogen bonds through hydration.[30] The Raman spectra of Al-LLZ sintered at 900 °C and 1200 °C (Fig. 3 (e and f)) were found to be similar to that of the high conductive cubic phase with distorted lithium sublattice. The PXRD and Raman spectra of the Al-LLZ sample sintered at 900 °C and 1200 °C confirm the stabilization of high conductive cubic phase.

PXRD patterns of Al-LLZ and Al-LLZ added with 1wt.% of Li_3BO_3, Li_3PO_4 and Li_4SiO_4 sintered at 900 °C for 36 h are presented in Fig. 4 (a-d). The PXRD patterns of these samples shown as Fig. 4 (a-d) matches well with the reported high temperature cubic phase LLZ. Additional weak impurity peaks corresponding to that of $AlPO_4$ was observed (Fig. 4 (c)) for the Al-LLZ added with 1wt.% of Li_3PO_4. Fig. 5 shows the PXRD pattern of Al-LLZ, Al-LLZ added with 1wt.% of Li_3PO_4 and Li_4SiO_4 sintered at 1200 °C along with the reported high conductive cubic phase LLZ.[4] No additional impurity peak was observed for the Al-LLZ added with 1wt.% of Li_4SiO_4. However an additional impurity peaks of $AlPO_4$ was observed in the PXRD pattern of Al-LLZ added with 1wt.% of Li_3PO_4. Although the Raman spectra of the Al-LLZ added with 1wt.% of Li_3BO_3 sintered at 900 °C and Al-LLZ added with 1wt.% of Li_3PO_4 and Li_4SiO_4 sintered at 1200 °C presented in Fig. 6 resemble the high conductive cubic phase Al-LLZ a close observation revealed minor change in the position and contour. The slight changes observed in the Raman and PXRD indicate the possible minor modification in the lattice of Al-LLZ with the loading of sintering additives.

3.2 Microstructural analysis

Typical SEM images of the fractured surface of Al-LLZ and Al-LLZ added with 1wt.% of Li_3BO_3, Li_3PO_4 and Li_4SiO_4 pellets sintered at 900 °C for 36 h are shown in Fig. 7 (a-d). Comparison of the SEM images shown in Fig 7 (a-d) revealed no dramatic improvement in the density with the addition of sintering additives at this sintering temperature. Comparison of SEM images of Al-LLZ (Fig.7 (a)) and Al-LLZ added with 1wt.% of Li_3BO_3 (Fig.7 (b)) indicate the addition of Li_3BO_3 helps to slightly enhance the density. The segregation of possible secondary phase at the grain-boundaries of Al-LLZ added with 1wt.% of Li_3PO_4 is evidenced through the SEM images of Fig. 7 (c). Since the melting point of Li_4SiO_4 (1255 °C) is higher than that of Li_3PO_4 (873 °C) and Li_3BO_3 (700 °C), the sintering temperature of 900 °C is not sufficient to melt the Li_4SiO_4 hence it might be segregated in the grain-boundary as seen in Fig.7 (d).

The SEM images of fractured surface of Al-LLZ and Al-LLZ added with 1wt.% of Li_3PO_4 and Li_4SiO_4 sintered at 1200 °C are shown as Fig. 8 (a-c). The corresponding magnified SEM images are shown as Fig. 8 (d-f). The surface morphology on the fractured surfaces of Al-LLZ and Al-LLZ added with 1wt.% of Li_3PO_4 and Li_4SiO_4 shown in Fig. 8 (a-f) clearly revealed the difference between microstructure of the prepared pellets with different sintering additives. The addition of Li_3PO_4 introduces a significant change in microstructure of Al-LLZ as shown in Fig. 8 (b and e). The SEM images of Li_3PO_4 added Al-LLZ (Fig. 8 (b and e)) reveal the growth of well crystallized large grains and relatively better contact with the neighbouring grains, but certain amount of pores can be observed in between the grains. The magnified SEM image of the Li_3PO_4 added Al-LLZ Fig. 8 (e) also indicated the possible inclusion of secondary phase at the grain-boundaries. The FE-SEM image and EDX mapping of the fractured surface of Al-LLZ

added with 1wt.% of Li_3PO_4 sintered at 1200 °C are shown as Fig. S1 and S2 (ESI), respectively. The FE-SEM image of Al-LLZ added with 1wt.% of Li_3PO_4 given as Fig.S1 indicated the presence of secondary phase on the surface of the grains. The FE-SEM image and EDX mapping indicated the segregation of possible impurity phase $AlPO_4$ at the grain-boundary. The presence of $AlPO_4$ as secondary phase was also revealed by PXRD pattern of Al-LLZ added with 1wt.% of Li_3PO_4 sintered at 1200 °C. However, the SEM image of the fractured surface of Al-LLZ added with 1wt.% of Li_4SiO_4 (Fig. 8 (c and f)) indicated quite dense microstructure with small gas pores, implying that the viscous flow sintering occurred as a result of creation of liquid phase at the sintering temperature around 1200 °C.

Density of the prepared pellets were calculated using the formula

$$\rho = \frac{Wair}{Wair - Wwater} \text{ x } \rho water \qquad (1)$$

where

Wair is the weight of the sample in air (g),

Wwater is the weight of the sample in deionised water (g),

$\rho water$ is the density of deionised water (gcm^{-3}).

The calculated experimental density of Al-LLZ, Al-LLZ added with 1wt.% of Li_3BO_3, Li_3PO_4 and Li_4SiO_4 sintered at 900 °C and 1200 °C are tabulated in Table 1. Among the samples sintered at 900 °C, the Al-LLZ added with 1wt. % of Li_3BO_3 exhibits the maximized density of 3.96 gcm^{-3} (relative density 76%) and for the samples sintered at 1200 °C the maximized density of 4.86 gcm^{-3} (relative density 96%) was observed for Al-LLZ added with 1wt.% of Li_4SiO_4.

3.3 Impedance analysis

Fig. 9 shows the room temperature (33 °C) AC impedance plots of Al-LLZ, Al-LLZ added with 1wt.% of Li_3BO_3, Li_3PO_4 and Li_4SiO_4 sintered at 900 °C for 36 h. The real and imaginary parts of impedance (Z′(Ω) and Z″(Ω)) were multiplied by a factor of A/t (where A and t are surface area and thickness of the pellet, respectively) and are plotted in Fig. 9 as Z′(Ωcm) vs. Z″(Ωcm) for the purpose of the comparison of the samples with different geometrical sizes. The total (bulk + grain-boundary) Li^+ conductivity was calculated from the inverse of the resistivity derived from the intercepts of the high frequency semicircles with the real axis. The room temperature (33 °C) total (bulk + grain-boundary) Li^+ conductivity for the Al-LLZ, Al-LLZ added with 1wt.% of Li_3BO_3, Li_3PO_4 and Li_4SiO_4 sintered at 900 °C for 36 h are tabulated in Table 1. Among the samples sintered at 900 °C, the maximized room temperature (33 °C) total (bulk + grain-boundary) Li^+ conductivity was observed for the Al-LLZ added with 1wt.% of Li_3BO_3. The room temperature (33 °C) experimental impedance data points of Al-LLZ added with 1wt.% of Li_3BO_3 (sintered at 900 °C) were fitted with an equivalent circuit consisting of two parallel combination of resistances and constant phase elements (CPEs) representing the electrical bulk and grain-boundary contribution $(R_bCPE_b)(R_{gb}CPE_{gb})$ and presented as inset of Fig. 9. Corresponding capacitance value were calculated by using the formula

$$C = R^{\left(\frac{1-n}{n}\right)}Q^{\frac{1}{n}} \qquad (2)$$

where R represents the resistance, Q represents the constant phase element and n is the parameter with a value close to 1.

The bulk and total (bulk + grain-boundary) Li^+ conductivity of Al-LLZ added with 1wt.% of Li_3BO_3 sintered at 900 °C were estimated to be around 3.6 x 10^{-5} Scm^{-1} and 1.3 x 10^{-5} Scm^{-1}, respectively, which illustrate the enhancement in the total (bulk + grain-boundary) Li^+

conductivity by reducing the grain-boundary resistance. The melted Li_3BO_3 at the grain boundary could contribute to facile Li+ conduction between Al-LLZ grains. However no appreciable reduction in the grain-boundary resistance was observed with the addition of 1wt.% of Li_3PO_4 and Li_4SiO_4. The segregation of possible unfavourable secondary phase at the grain-boundaries might be the reason for the appreciable grain-boundary resistance observed in the case of Al-LLZ added with 1wt.% of Li_3PO_4. The sintering temperature of 900 °C might not be sufficient to melt the Li_4SiO_4 and hence they segregate at the grain-boundary and do not help to decrease the grain-boundary resistance.

As the melting point of Li_3BO_3 is low (700 °C), the Al-LLZ added with 1wt.% of Li_3BO_3 was not considered further for sintering to 1200 °C. The AC impedance plots for the Al-LLZ, Al-LLZ added with 1wt.% of Li_3PO_4 and Li_4SiO_4 sintered at 1200 °C measured in the room temperature (33 °C) are shown as Fig. 10 (a-c). Although the AC impedance plots shown in Fig. 10 (a-c) exhibit a tail in the low frequency region representing the electrode polarization effects, the contributions from the grain and grain-boundary could not be distinguished clearly in the high frequency region. The experimental frequency dependant data of Al-LLZ and Al-LLZ added with 1wt.% of Li_3PO_4 were quantitatively analyzed with a suitable equivalent circuit using individual resistances and constant phase elements (CPEs) representing the electrical bulk, grain-boundary and electrode response, respectively, (R_bCPE_b) ($R_{gb}CPE_{gb}$) (CPE_{el}) (Fig.10 (a) and inset of Fig. 10 (b)) and the resultant fitting parameters are listed in Table 2. The AC impedance plot for the Al-LLZ added with 1wt.% of Li_4SiO_4 shown as Fig. 10 (c) revealed that the bulk and grain-boundary contribution could not be resolved clearly which indicates negligible grain-boundary resistance in that sample. Hence, the corresponding impedance plot was fitted with the suitable equivalent circuit using individual resistances and constant phase element (CPE)

representing the total (bulk + grain-boundary) and electrode response, respectively, (RCPE) (CPE_{el}) shown as inset of Fig.10 (c). Among the investigated samples the Al-LLZ added with 1wt.% of Li_4SiO_4 sintered at 1200 °C exhibits the maximized total (bulk + grain-boundary) Li^+ conductivity of 6.1 x 10^{-4} Scm^{-1}.

To increase the total conductivity, the grain-boundary resistivity should be reduced. One possible approach is to decrease the thickness of grain-boundary. The thickness of the grain-boundary may be reduced by increasing the grain size by grain growth. However, the increase of grain size alone may not be enough to enhance the grain-boundary conductivity. The other approach is obtaining the grain-boundary of lower resistance by modifying the high conductive grain-boundary composition. As revealed by SEM investigations, although the addition of Li_3PO_4 helps to increase the growth of large grains, the total (bulk + grain-boundary) Li^+ conductivity was found to be reduced by the segregation of possible secondary phase $AlPO_4$ at the grain-boundary. On the other hand the addition of Li_4SiO_4 helps to enhance the density, reduce the grain-boundary resistance and thereby enhance the total (bulk + grain-boundary) Li^+ conductivity. The Si^{4+} from Li_4SiO_4 might replace some of the Al^{3+} /Li^+ in Al-LLZ, which may lead to Al^{3+} /Li^+ extraction from the bulk into the grain-boundary region for the formation of favourable Li^+ conducting thin layer with the possible combination of Li-Al-Si-O in the grain-boundary. Hence the increased numbers of empty structural sites in Al-LLZ lattice could permit increased Li^+ mobility and thus result into an increase in bulk conductivity and simultaneous enhancement in the grain-boundary conductivity through the favourable Li^+ conducting Li-Al-Si-O phase at the grain-boundary. On the other hand the segregation of unfavourable $AlPO_4$ at the grain-boundaries in the case of Al-LLZ added with 1wt.% of Li_3PO_4 might result into low total (bulk + grain-boundary) Li^+ conductivity.

Fig. 11 shows the Arrhenius plots for total (bulk + grain-boundary) Li^+ conductivity of Al-LLZ and Al-LLZ added with 1wt.% of Li_3BO_3, Li_3PO_4 and Li_4SiO_4 sintered at different elevated temperature measured in the temperature range from 33 to 240 °C. The entire samples were found to be thermally stable without any phase transition in the observed temperature range. The activation energies (E_a) for the total (bulk + grain-boundary) Li^+ conductivity of Al-LLZ, Al-LLZ added with 1wt.% of Li_3BO_3, Li_3PO_4 and Li_4SiO_4 in the temperature range of 33 to 240 °C can be determined from the Arrhenius plots by employing the equation

$$\sigma T = A \exp\left(\frac{-E_a}{kT}\right) \quad (3)$$

where A is the pre-exponential parameter, k is Boltzmann's constant and T is the absolute temperature. E_a was determined from the slope of the log (σT) vs. 1000/T plot.

The variation in room temperature (33 °C) bulk and total (bulk + grain-boundary) Li^+ conductivity and activation energy (total Li^+ conductivity) of Al-LLZ and Al-LLZ added with 1wt.% of Li_3BO_3, Li_3PO_4 and Li_4SiO_4 sintered at different elevated temperature is depicted in Fig. 12. The total (bulk + grain-boundary) Li^+ conductivity is found to be maximum along with the minimum activation energy for the Al-LLZ added with 1wt.% of Li_4SiO_4 sintered at 1200 °C. The changes observed in the bulk conductivity of Al-LLZ with the loading of sintering additives might be due to the slight changes in the composition of Al-LLZ. The Si/P/B from the sintering additives might replaces some of the Li^+/Al^{3+} which may lead to extraction of Li^+/Al^{3+} from the bulk (via charge compensation for the above substitution) through the incorporation of Si/P/B into the lattice. However further detailed studies are essential to understand the incorporation of Si/P/B into the LLZ lattice sites and its role on slight changes observed in the bulk conductivity.

A detailed comparison of the influence of sintering additives on total (bulk + grain-boundary) Li^+ conductivity and density of the investigated Al-LLZ lithium garnets along with the available data in the literature are provided as Table 3.

4 Conclusions

Al doped LLZ in cubic phase was successfully synthesized at relatively lower temperature around 900 °C by modified sol-gel technique and the influence of addition of sintering additives Li_3BO_3, Li_3PO_4 and Li_4SiO_4 on the density, microstructure and total (bulk + grain-boundary) Li^+ conductivity of Al doped LLZ were also investigated. The PXRD pattern and Raman spectra revealed that the incorporation of 0.9 wt.% Al into the LLZ helps to stabilize high conductive cubic phase at low sintering temperature. Among the samples Al-LLZ, Al-LLZ added with 1wt.% of Li_3BO_3, Li_3PO_4 and Li_4SiO_4 pellets sintered at 900 °C, the maximized room temperature (33 °C) total (bulk + grain-boundary) Li^+ conductivity of 1.3 x 10^{-5} Scm^{-1} and maximized density of 3.96 gcm^{-3} was observed for the Al-LLZ added with 1wt.% of Li_3BO_3. SEM investigations revealed that the Al-LLZ added with 1wt.% of Li_4SiO_4 sintered at 1200 °C was found to be relatively dense and indicate that Li_4SiO_4 acts as a better sintering agent compared to that of Li_3BO_3 and Li_3PO_4. Among the investigated samples Al-LLZ added with 1wt.% of Li_4SiO_4 sintered at 1200 °C exhibits the maximized room temperature (33 °C) total (bulk + grain-boundary) Li^+ conductivity of 6.1 x 10^{-4} Scm^{-1} and maximized density of 4.86 gcm^{-3} (relative density 96%). Further optimization of parameters like the amount of Li_4SiO_4 addition, sintering temperature and durations are essential to derive dense, gas pores free and high Li^+ conductive cubic phase Al-LLZ for the successful application of Al-LLZ as solid electrolyte membrane in all-solid-state lithium battery.

Acknowledgments

The authors thank Pondicherry University, Puducherry, India [PU/PC/Start-up Grant/2011-12/306] and BRNS, DAE, Mumbai, India [No. 37(3)/14/42/2014-BRNS] for the financial support.

References

1 V. Thangadurai, V. Kaack and W. Weppner, *J. Am. Ceram. Soc.,* 2003, **86**, 437.

2 V. Thangadurai, S. Adams and W. Weppner, *Chem. Mater.,* 2004, **16**, 2998.

3 V. Thangadurai and W. Weppner, *Adv. Funct. Mater.,* 2005, **15**, 107.

4 R. Murugan, V. Thangadurai and W. Weppner, *Angew. Chem. Int. Ed.,* 2007, **46**, 7778.

5 S. Kumazaki, Y. Iriyama, K.H. Kim, R. Murugan, K. Tanabe, K. Yamamoto, T. Hirayama and Z. Ogumi, *Electrochem. Commun.,* 2011, **13**, 509.

6 J. Awaka, N. Kijima, H. Hayakawa and J. Akimoto, *J. Solid State Chem.,* 2009, **182**, 2046.

7 J. Awaka, A. Takashima, K. Kataoka, N. Kijima, Y. Idemoto and J. Akimoto, *Chem. Lett.,* 2011, **40**, 60.

8 C. A. Geiger, E. Alekseev, B. Lazic, M. Fisch, T. Armbruster, R. Langner, M. Fechtelkord, N. Kim, T. Pettke and W. Weppner, *Inorg. Chem.,* 2011, **50**, 1089.

9 M. Kotobuki, K. Kanamura, Y. Sato and T. Yoshida, *J. Power Sources,* 2011, **196**, 7750.

10 A. Duevel, A. Kuhn, L. Robben, M. Wilkening and P. Heitjans, *J. Phys. Chem. C,* 2012, **116**, 15192.

11 H. Buschmann, J. Do¨ lle, S. Berendts, A. Kuhn, P. Bottke, M. Wilkening, P. Heitjans, A. Senyshyn, H. Ehrenberg, A. Lotnyk, V. Duppel, L. Kienle and J. Janek, *Phys. Chem. Chem. Phys.,* 2011, **13**, 19378.

12 E. Rangasamy, J. Wolfenstine and J. Sakamoto, *Solid State Ionics,* 2012, **206**, 28.

13 Y. X. Gao, X. P. Wang, W. G. Wang and Q. F. Fang, *Solid State Ionics,* 2010, **181**, 33.

14 Y. X. Gao, X. P Wang, W. G. Wang, Z. Zhuang, D. M. Zhang and Q. F. Fang, *Solid State Ionics,* 2010, **181**, 1415.

15 Y. Shimonishi, A. Toda, T. Zhang, A. Hirano, N. Imanishi, O. Yamamoto and Y. Takeda, *Solid State Ionics,* 2011, **183**, 48.

16 I. Kokal, M. Somer, P. H. L. Notten and H. T. Hintzen, *Solid State Ionics,* 2011, **185**, 42.

17 Y. Jin and P. J. Mcginn, *J. Power Sources,* 2011, **196**, 8683.

18 N. Janani, S. Ramakumar, L. Dhivya, C. Deviannapoorani, K. Saranya and R. Murugan, *Ionics,* 2011, **17**, 575.

19 R. Takano, K. Tadanaga, A. Hayashi and M. Tatsumisago, Solid State Ionics, 2012, 206, 28-32.

20 C. Yang, L. Y. Qiu and G. X. Xin, *Chin. Phys. B,* 2013, **22**, 078201.

21 Y. Li, Y. Cao and X. Guo, *Solid State Ionics,* 2013, **253**, 76.

22 Y. Li, Z. Wang, C. Li, Y. Cao and X. Guo, *J. of Power Sources,* 2014, **248**, 642.

23 X. Wu, Z. Wen, X. Xu, X. Wang and J. Lin, *J. of Nucl. Mater.,* 2009, **392**, 471.

24 K. Saranya, C. Deviannapoorani, L. Dhivya, S. Ramakumar, N. Janani and R. Murugan, *Mater. Lett.,* 2012, **77**, 57.

25 C. Julien, *Ionics,* 2000, **6**, 30.

26 C. M. Julien and M. Massot, *Mater. Sci. Eng. B,* 2003, **100**, 69.

27 G. Larraz, A. Orera and M. L. Sanjuan, *J. Mater. Chem. A,* 2013, **1**, 11419.

28 F. Tietz, T. Wegener, M. T. Gerhards, M. Giarola and G. Mariotto, *Solid State Ionics,* 2013, **230**, 77.

29 S. Ramakumar, L. Satyanarayana, S. V. Manorama and R. Murugan, *Phys. Chem. Chem. Phys.,* 2013, **15**, 11327.

30 C. Galven, J. Dittmer, E. Suard, F. Le Berre and M. P. Crosnier-Lopez, *Chem. Mater.,* 2012, **24**, 3335.

Table 1 Room temperature (33 °C) bulk and total (bulk + grain-boundary) Li^+ conductivity, activation energy (in the temperature range 33 to 240 °C) and density of Al-LLZ and Al-LLZ added with 1wt.% of Li_3BO_3, Li_3PO_4 and Li_4SiO_4 sintered at 900 °C and 1200 °C.

Compound	Sintering Temperature	σ_{bulk}(Scm^{-1}) 33 °C	σ_{total}(Scm^{-1}) 33 °C	Activation Energy (E_a) eV	Density (gcm^{-3})
Al-LLZ	900 °C	-	3.0×10^{-7}	-	3.33
Al-LLZ + LB	900 °C	3.6×10^{-5}	1.3×10^{-5}	0.41	3.96
Al-LLZ + LP	900 °C	-	3.4×10^{-7}	-	3.80
Al-LLZ + LS	900 °C	-	4.3×10^{-7}	-	3.84
Al-LLZ	1200 °C	2.1×10^{-4}	1.1×10^{-4}	0.38	3.99
Al-LLZ + LP	1200 °C	5.5×10^{-4}	3.5×10^{-4}	0.36	4.05
Al-LLZ + LS	1200 °C	6.1×10^{-4}	6.1×10^{-4}	0.34	4.86

Table 2 Parameters obtained from the fitting of room temperature (33 °C) experimental AC impedance data of Al-LLZ and Al-LLZ added with 1wt.% of Li_3BO_3, Li_3PO_4 and Li_4SiO_4 sintered at different elevated temperature by using suitable equivalent circuit elements.

Compound	R_b (Ωcm)	C_b (F)	R_{gb} (Ωcm)	C_{gb} (F)	R_{gb}/R_{total} [a]
Al-LLZ + LB (900-36h)	27570	1.7×10^{-10}	47490	7.6×10^{-9}	0.63
Al-LLZ (1200-12h)	4676	5.1×10^{-10}	4676	1.8×10^{-9}	0.50
Al-LLZ + LP (1200-12h)	1831	-	986	5.9×10^{-9}	0.35
Al-LLZ + LS (1200-12h)	1632*	$4.5 \times 10^{-10*}$	-	-	-

[a] $R_{total} = R_{bulk} + R_{grain\text{-}boundary}$

* Unable to resolve the grain-boundary contribution

Table 3 Comparison of influence of sintering additives on total (bulk + grain-boundary) Li^+ conductivity and density of LLZ and Al-LLZ lithium garnets.

Nominal composition	Synthesis technique	Sintering condition	Sintering additive	σ_{total} (Scm^{-1})	Experimental density gcm^{-3}	Relative density %	Ref.
LLZ	Solid-State	1230°C,36h	-	5×10^{-4} (25 °C)	-	92	[4]
LLZ	Solid-State	1230°C, 36h	1.3 wt.% Al	2.4×10^{-4} (25 °C)	4.45	-	[5]
LLZ	Solid-State	1230°C,36h	1.7wt.% Al and 0.1wt.% Si	6.8×10^{-4} (25 °C)	4.76	93	[5]
Al-LLZ	Pechini	1200°C,6h	1.2wt.% Al	2×10^{-4} (RT)	4.40	-	[17]
Al-LLZ	Sol-gel	900°C,10h	0.68 molar ratio Li_3BO_3	1.9×10^{-5} (RT)	-	-	[19]
Al-LLZ	Sol-gel	900°C,36h	1wt.% Li_3BO_3	1.3×10^{-5} (33 °C)	3.96	76	Present work
Al-LLZ	Sol-gel	1200°C,12h	1wt.% Li_3PO_4	3.5×10^{-4} (33 °C)	4.05	79	Present work
Al-LLZ	Sol-gel	1200°C,12h	1wt.% Li_4SiO_4	6.1×10^{-4} (33 °C)	4.86	96	Present work

Figure Captions

Fig. 1 Flow chart for the preparation of Al-LLZ by modified sol-gel technique and Al-LLZ added with 1wt.% of Li_3BO_3, Li_3PO_4 and Li_4SiO_4.

Fig. 2 PXRD patterns for the precursor of LLZ sintered at (a) 700 °C, (b) 800 °C, (c) 900 °C, (d) LLZ pellet sintered at 800 °C exposed to humid condition and the precursors of Al-LLZ sintered at (e) 900 °C and (f) 1200 °C along with the reported pattern of cubic LLZ and tetragonal LLZ[4, 6] (* denotes $La_2Zr_2O_7$, ^{o} denotes La_2O_3 and $^{\#}$ denotes $LaAlO_3$ impurity peaks).

Fig. 3 Raman spectra for the precursors of LLZ sintered at (a) 700 °C, (b) 800 °C, (c) 900 °C, (d) LLZ pellet sintered at 800 °C exposed to humid condition and the precursors of Al-LLZ sintered at (e) 900 °C and (f) 1200 °C along with the reported pattern of cubic LLZ[30] and tetragonal LLZ in the range 75-1000 cm^{-1}.

Fig. 4 PXRD patterns of (a) Al-LLZ, (b) Al-LLZ added with 1wt.% of Li_3BO_3, (c) Al-LLZ added with 1wt.% of Li_3PO_4 and (d) Al-LLZ added with 1wt.% of Li_4SiO_4 sintered at 900 °C along with the reported pattern of cubic LLZ[4] (* denotes $AlPO_4$ impurity peaks).

Fig. 5 PXRD patterns of (a) Al-LLZ, (b) Al-LLZ added with 1wt.% of Li_3PO_4 and (c) Al-LLZ added with 1wt.% of Li_4SiO_4 sintered at 1200 °C along with the reported pattern of cubic LLZ[4] (* denotes $AlPO_4$ impurity peaks).

Fig. 6 Raman spectra of (a) Al-LLZ sintered at 1200 °C, (b) Al-LLZ added with 1wt.% of Li_3BO_3 sintered at 900 °C, (c) Al-LLZ added with 1wt.% of Li_3PO_4 sintered at 1200 °C and (d) Al-LLZ added with 1wt.% of Li_4SiO_4 sintered at 1200 °C.

Fig. 7 SEM images for the fractured surfaces of (a) Al-LLZ, (b) Al-LLZ added with 1 wt.% of Li_3BO_3, (c) Al-LLZ added with 1 wt.% of Li_3PO_4 and (d) Al-LLZ added with 1 wt.% of Li_4SiO_4 sintered at 900 °C.

Fig. 8 SEM images of the fractured surfaces of (a) Al-LLZ, (b) Al-LLZ added with 1 wt.% of Li_3PO_4 (c) Al-LLZ added with 1 wt.% of Li_4SiO_4 sintered at 1200 °C and (d-f) represent corresponding magnified SEM images, respectively.

Fig. 9 Typical room temperature (33 °C) AC impedance plots of Al-LLZ and Al-LLZ added with 1wt.% of Li_3BO_3, Li_3PO_4 and Li_4SiO_4 pellets sintered at 900 °C using Li^+ blocking Au electrodes. The inset shows the profile for Al-LLZ added with 1wt.% of Li_3BO_3 and the corresponding fitting curve. The solid line represents the fitted data with an equivalent circuit consisting of two parallel combination of resistance and constant phase elements (CPEs) representing the electrical bulk and grain-boundary contribution, respectively, (R_bCPE_b) ($R_{gb}CPE_{gb}$) (where R is the resistance and CPE is the constant phase element and the subscript b and gb refers to the bulk and grain-boundary contribution, respectively).

Fig. 10 (a) Typical room temperature (33 °C) AC impedance plots of Al-LLZ pellet sintered at 1200 °C using Li^+ blocking Au electrodes. The solid line represents the fitted data with an equivalent circuit provided in the figure. The two semi-circles (dotted line) below the fitting curve illustrate the separation of two contributions from bulk and grain boundary, respectively.

(b) Typical room temperature (33 °C) AC impedance plots of Al-LLZ added with 1wt.% of Li_3PO_4 pellet sintered at 1200 °C using Li^+ blocking Au electrodes. The impedance data in the

high frequency region of Al-LLZ added with 1wt.% of Li_3PO_4, the corresponding fitting curve (solid line) and an equivalent circuit are shown as inset.

(c) Typical room temperature (33 °C) AC impedance plots of Al-LLZ added with 1wt.% of Li_4SiO_4 pellet sintered at 1200 °C using Li^+ blocking Au electrodes. The impedance data in the high frequency region of Al-LLZ added with 1wt.% of Li_4SiO_4 the corresponding fitting curve (solid line) and an equivalent circuit are shown as inset.

Fig. 11 Arrhenius plots for the total (bulk + grain-boundary) Li^+ conductivity of Al-LLZ and Al-LLZ added with 1wt.% of Li_3BO_3, Li_3PO_4 and Li_4SiO_4 sintered at different elevated temperature measured in the temperature range from 33 to 240 °C.

Fig. 12 The composition dependencies of bulk and total Li^+ conductivity measured at 33 °C and activation energy (total Li^+ conductivity) of Al-LLZ added with 1wt.% of Li_3BO_3 sintered at 900 °C, Al-LLZ sintered at 1200 °C, Al-LLZ added with 1wt.% of Li_3PO_4 sintered at 1200 °C and Al-LLZ added with 1wt.% of Li_4SiO_4 sintered at 1200 °C.

Figures

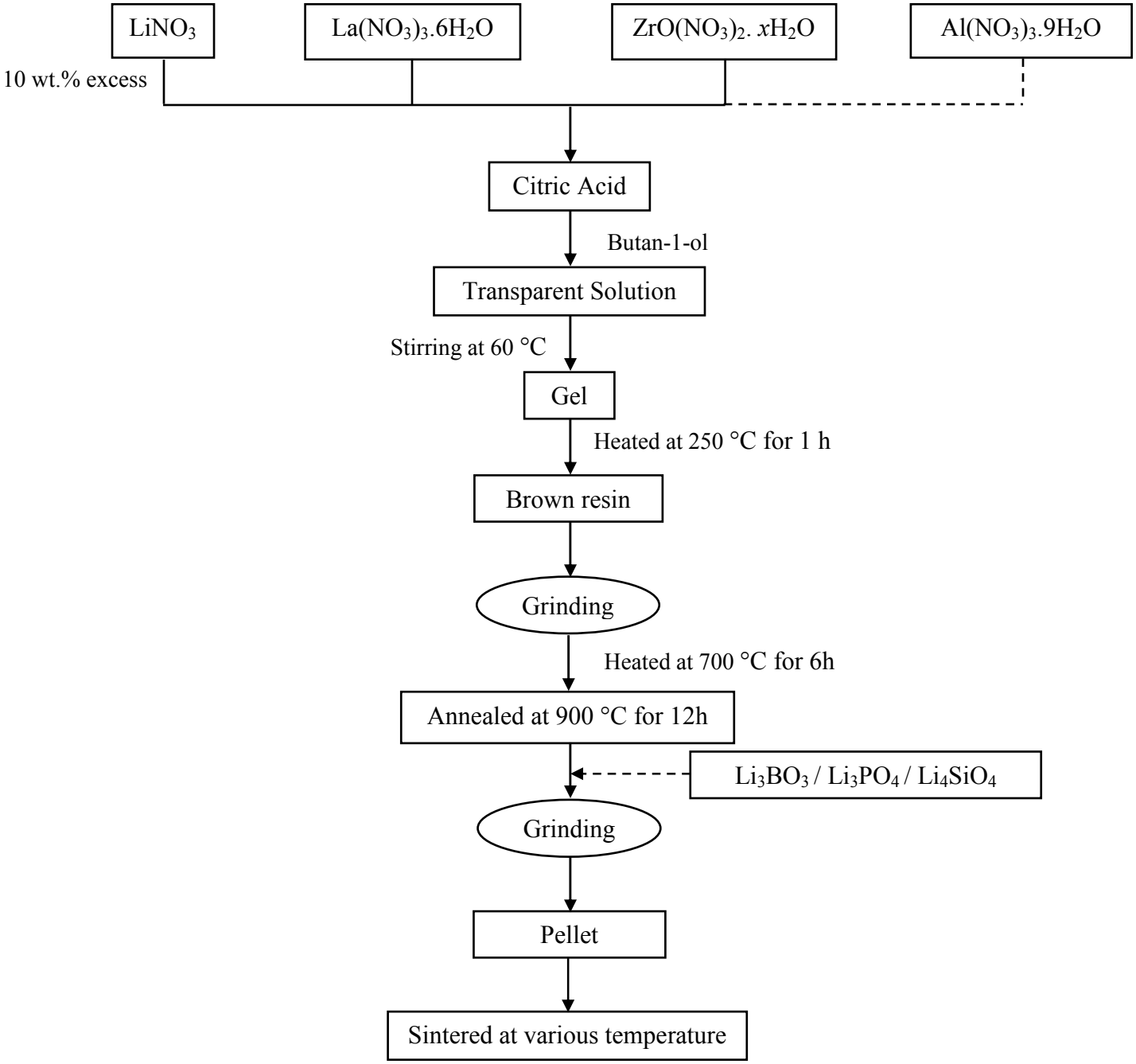

Fig. 1

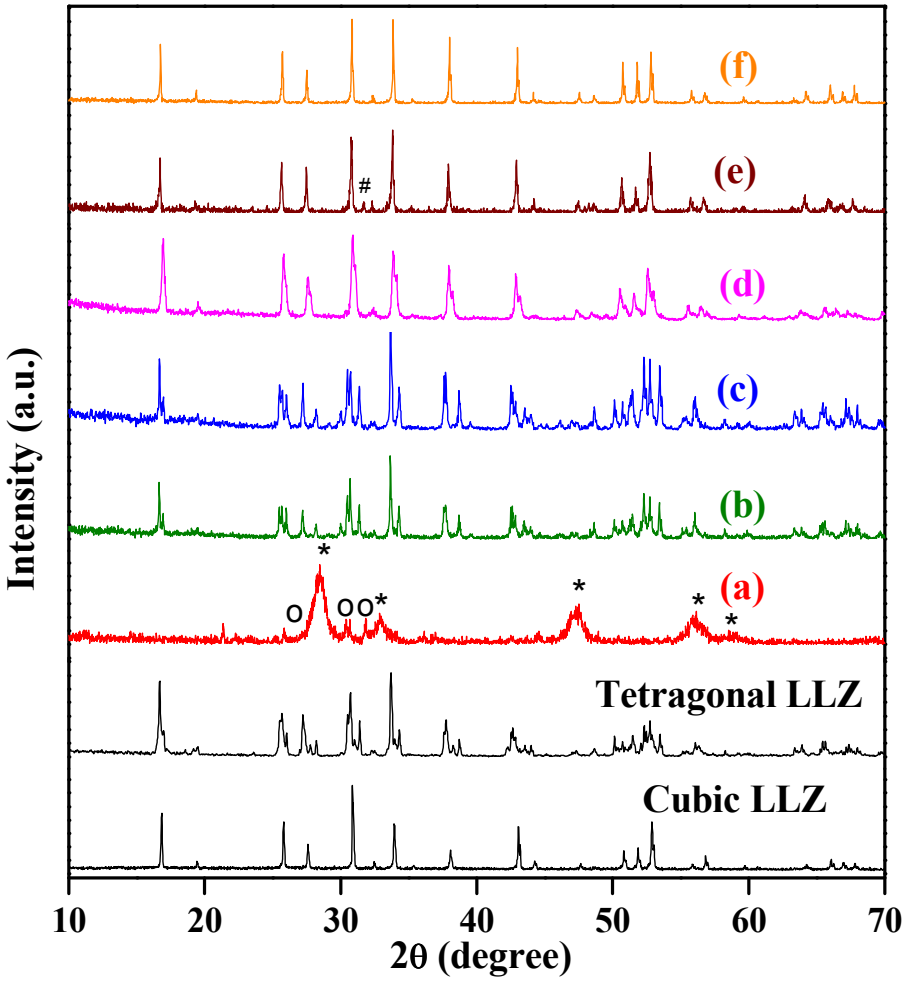

Fig. 2

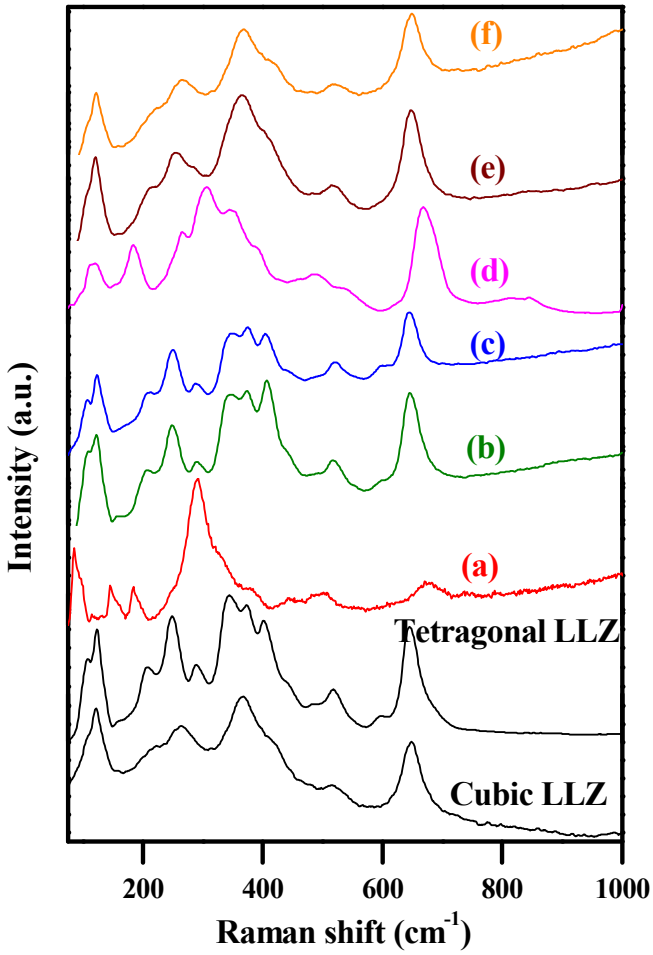

Fig. 3

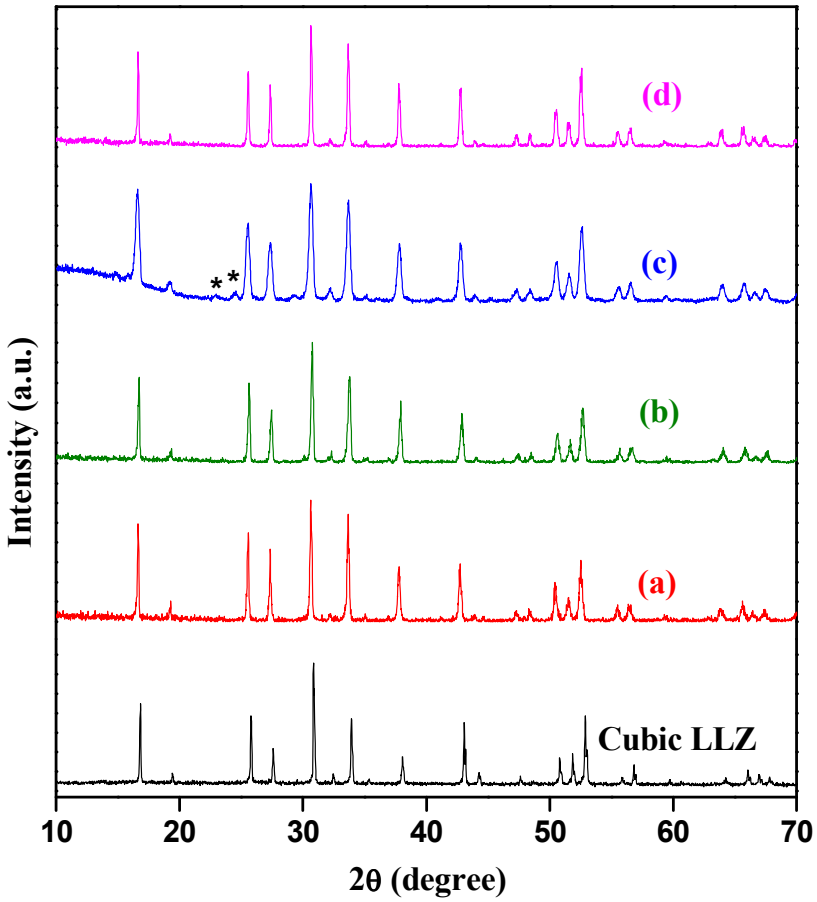

Fig. 4

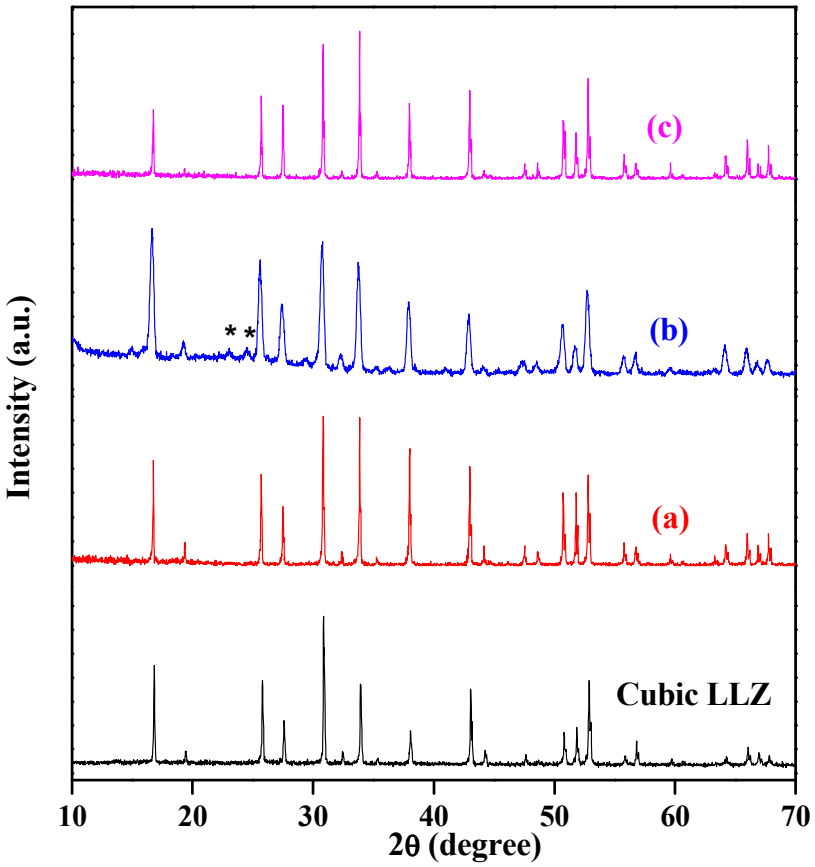

Fig. 5

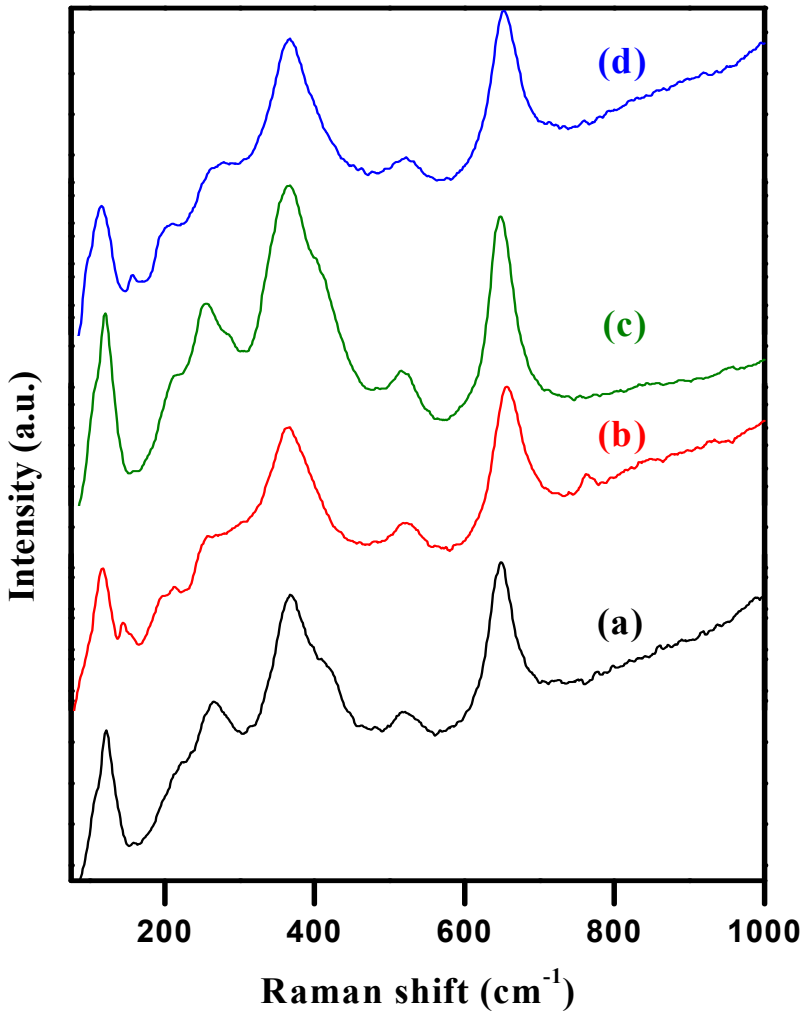

Fig. 6

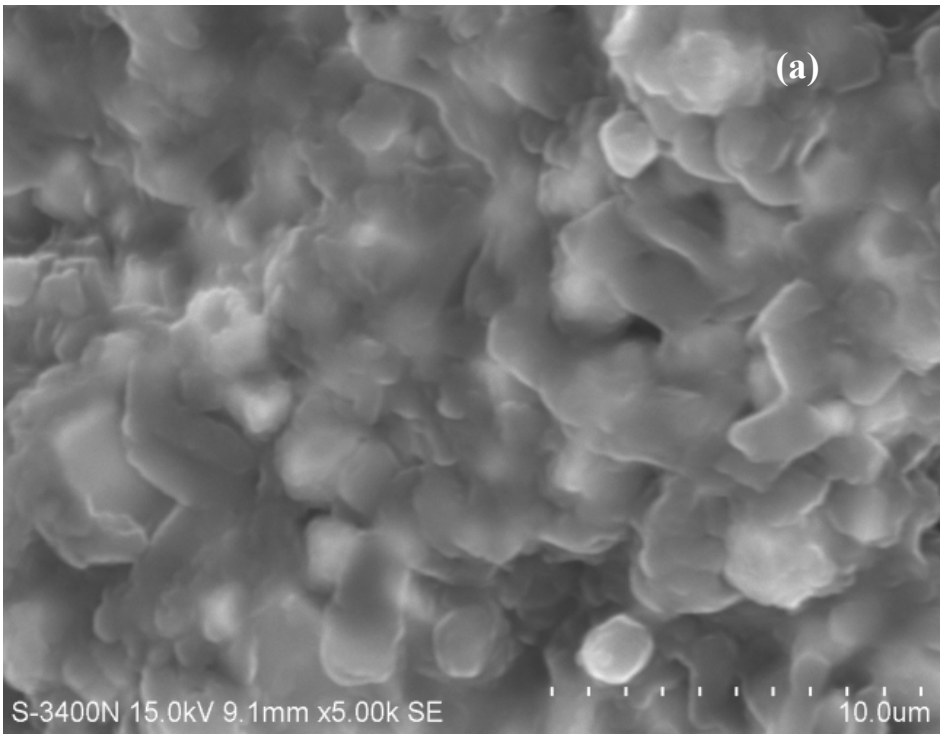

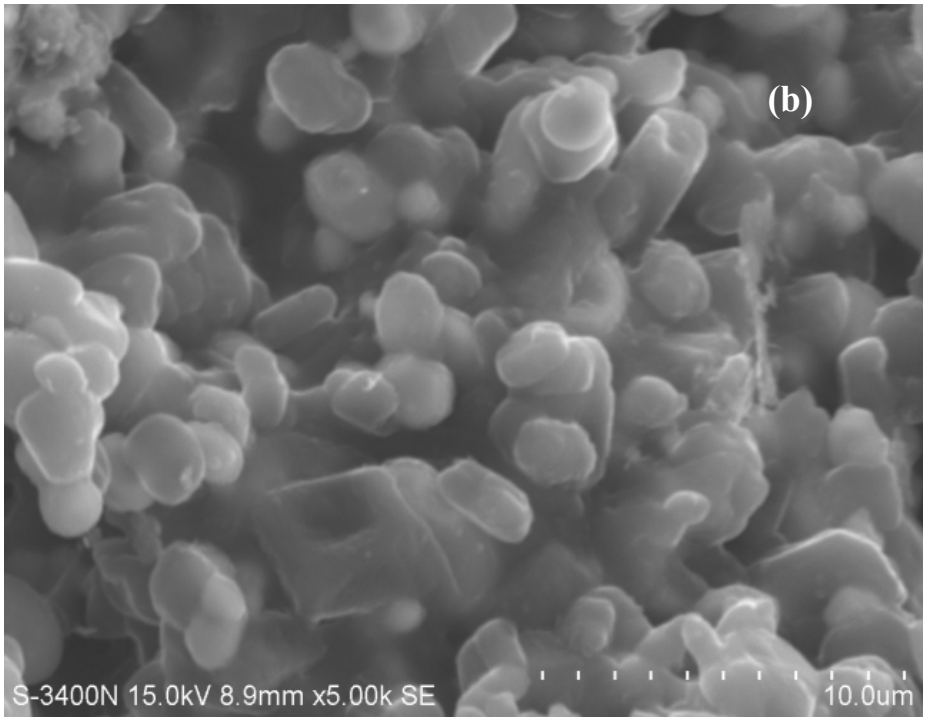

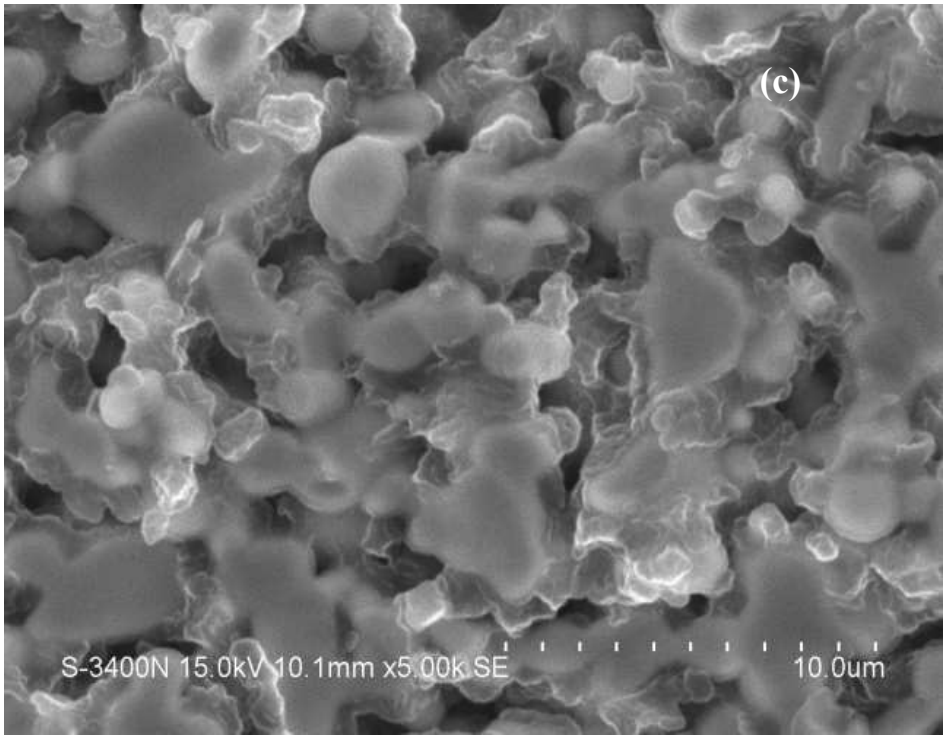

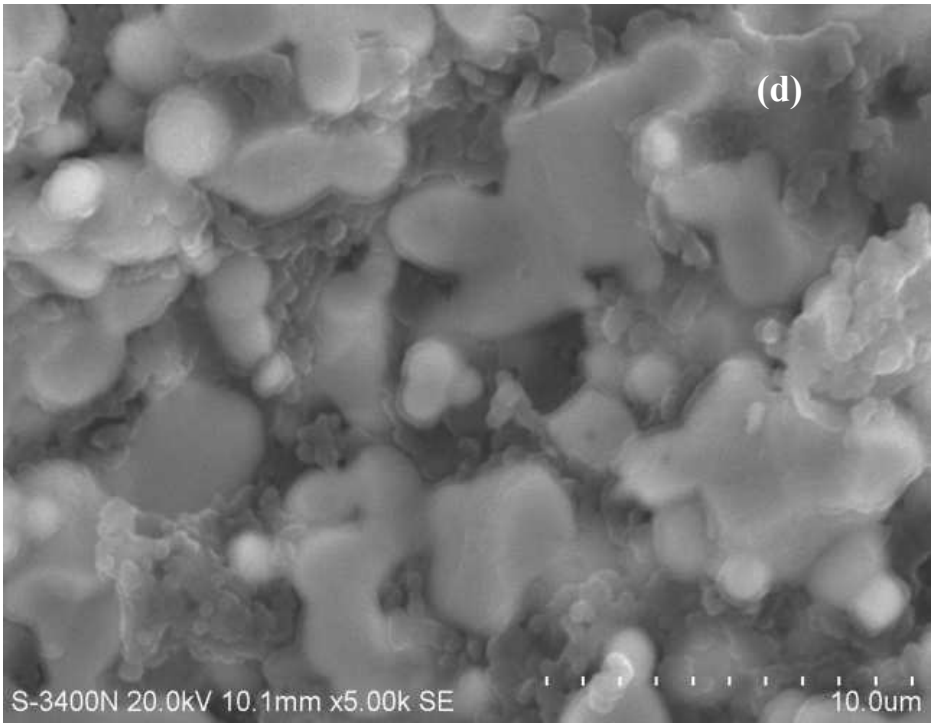

Fig. 7(a-d)

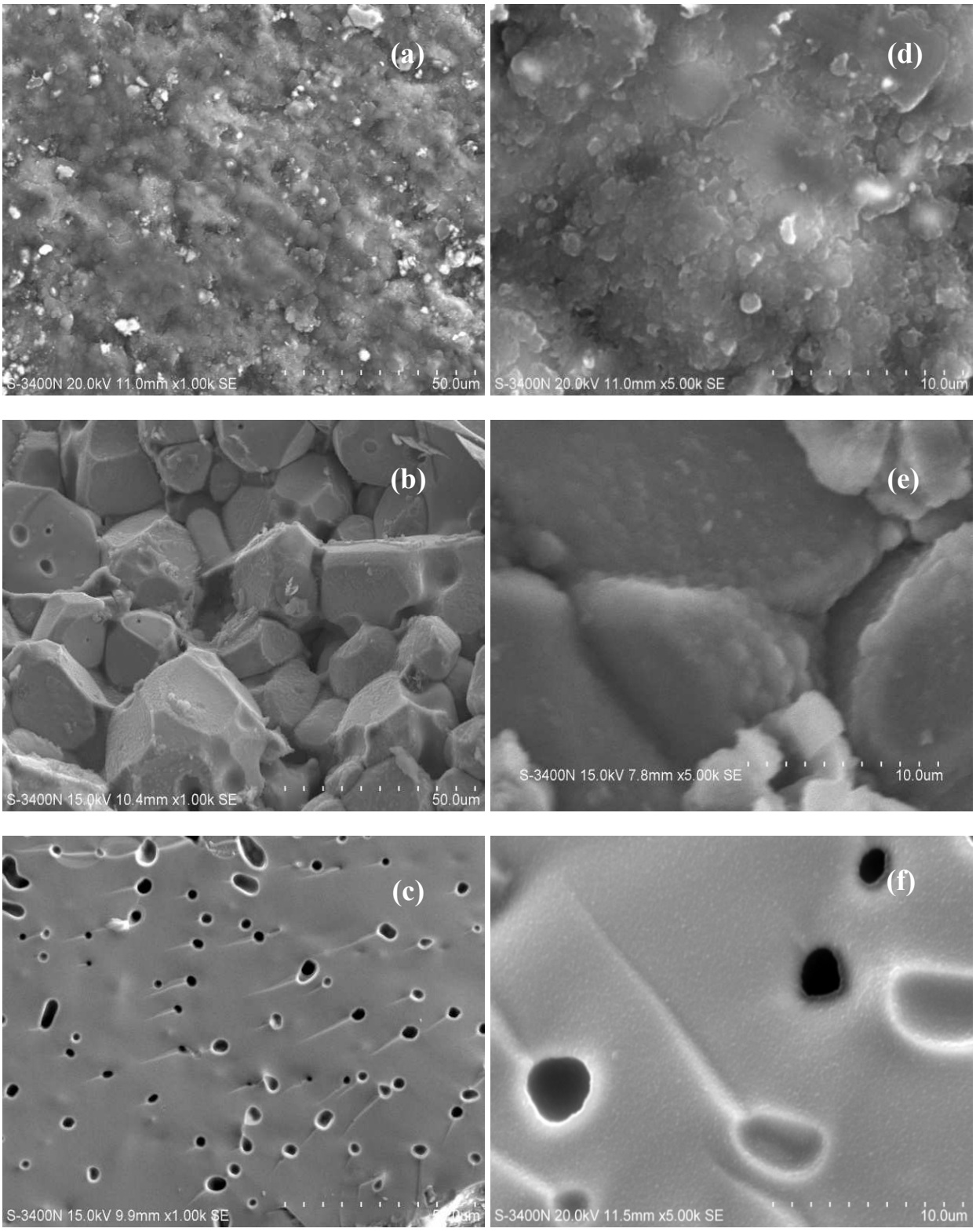

Fig. 8

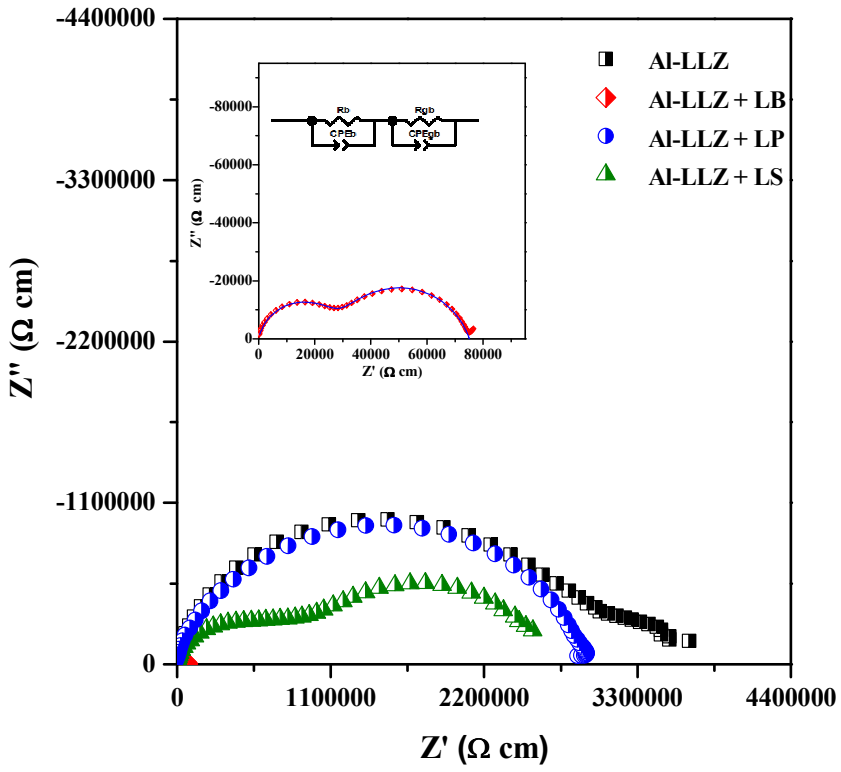

Fig. 9

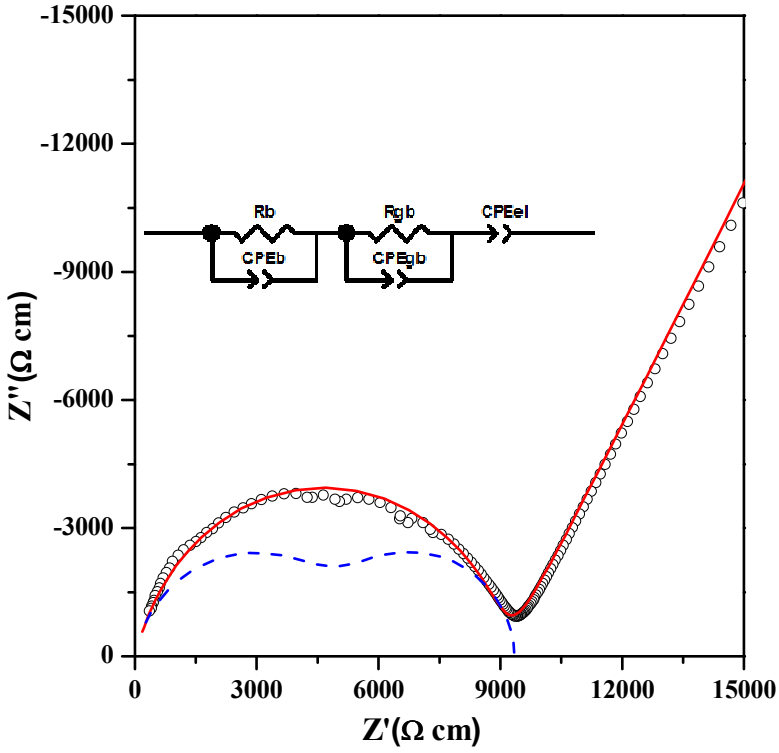

Fig. 10 (a)

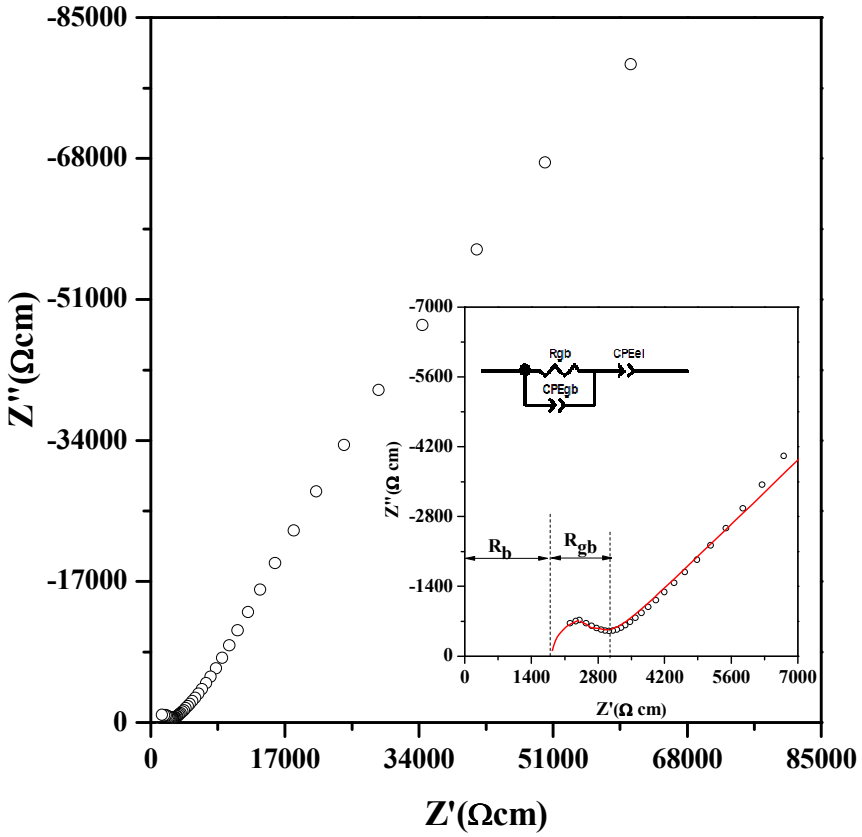

Fig. 10 (b)

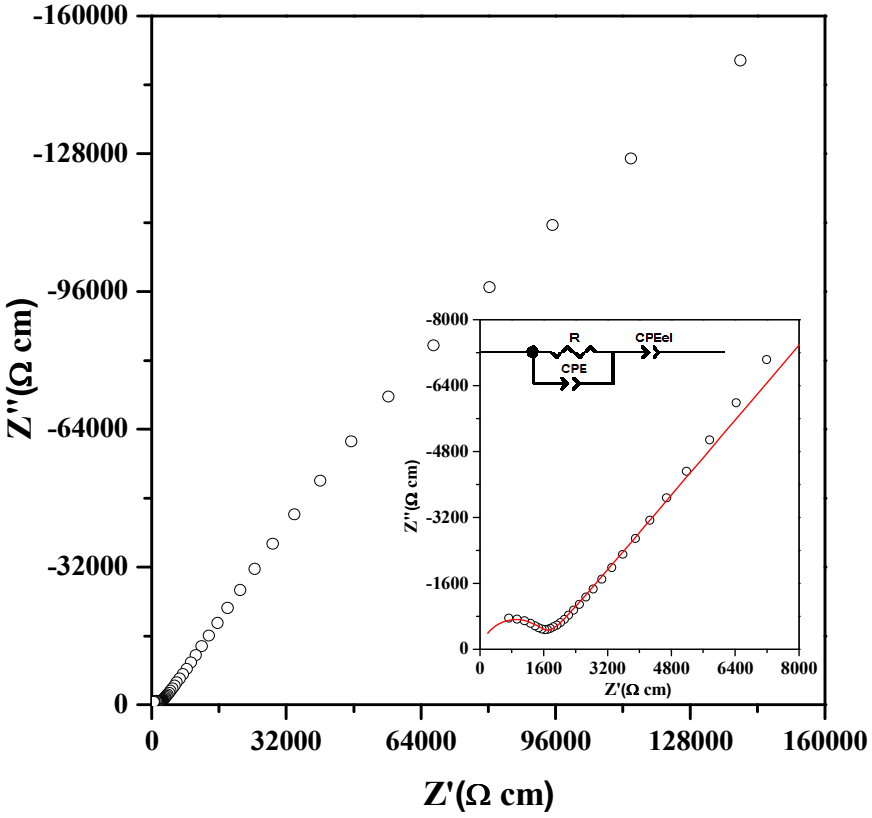

Fig. 10 (c)

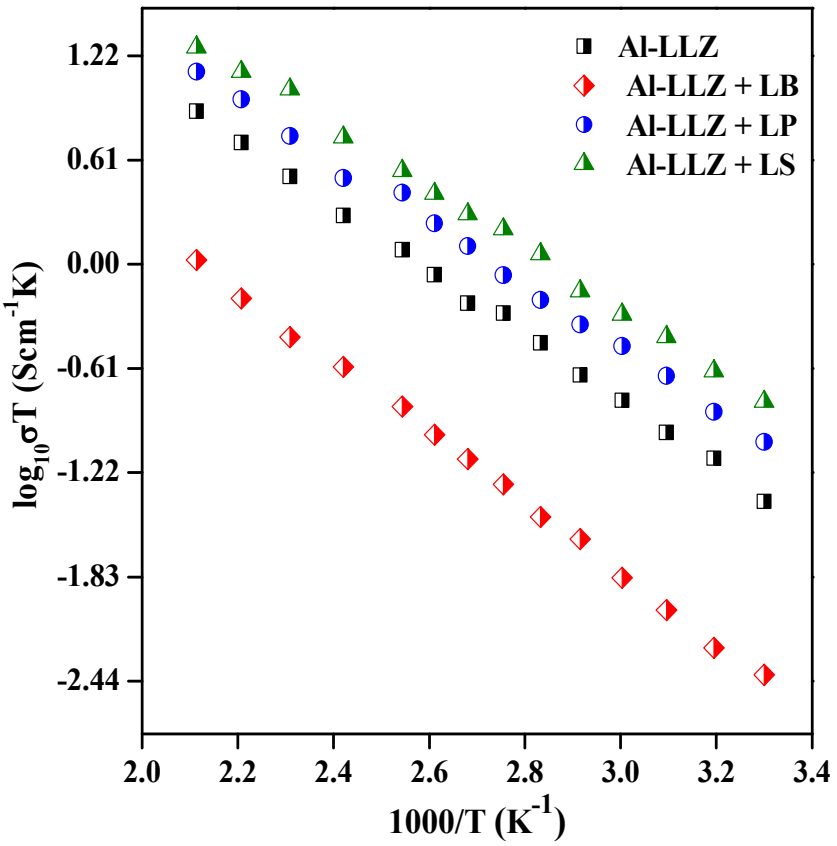

Fig. 11

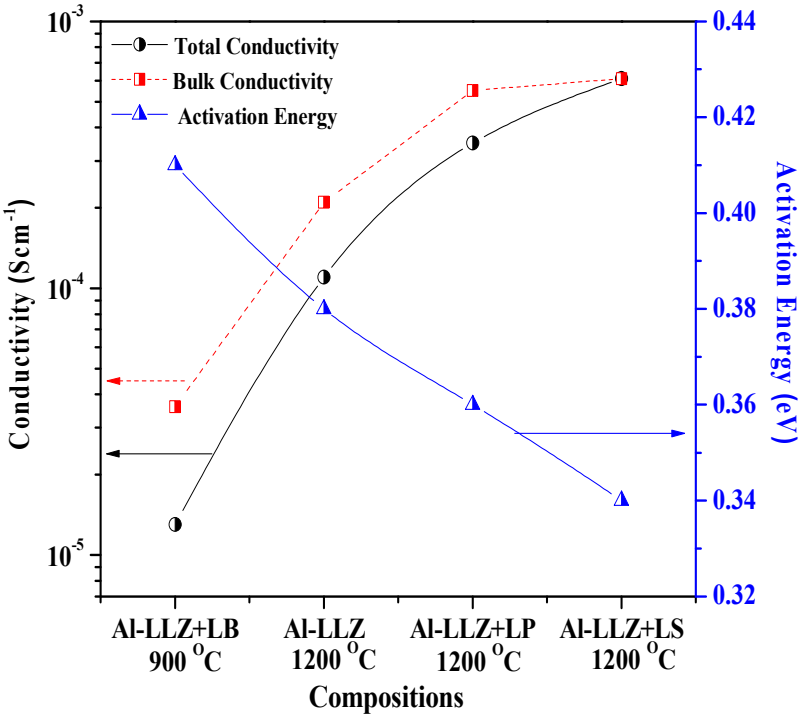

Fig. 12

Table of contents

Al-LLZ added with 1wt.% of Li_4SiO_4 sintered at 1200 °C was found to be relatively dense which enhances the total (bulk + grain-boundary) Li^+ conductivity by reducing the grain-boundary contribution.